ACS APPLIED MATERIALS & INTERFACES

Research Article

www.acsami.org

Fe–Cr–Al Containing Oxide Semiconductors as Potential Solar Water-Splitting Materials

Kirill Sliozberg,[†] Helge S. Stein,[‡] Chinmay Khare,[‡] Bruce A. Parkinson,[§] Alfred Ludwig,*[,‡,∥] and Wolfgang Schuhmann*[,†,∥]

[†]Analytical Chemistry, Center for Electrochemical Sciences (CES), Ruhr-Universität Bochum, Universitätsstrasse 150; D-44780 Bochum, Germany

[‡]Chair for MEMS Materials, Institute for Materials, Ruhr-Universität Bochum, Universitätsstrasse 150, D-44780 Bochum, Germany

[§]Department of Chemistry and School of Energy Resources, University of Wyoming, Laramie, Wyoming 82071, United States

[∥]Materials Research Department, Ruhr-Universität Bochum, Universitätsstrasse 150, D-44780 Bochum, Germany

Supporting Information

ABSTRACT: A high-throughput thin film materials library for Fe–Cr–Al-O was obtained by reactive magnetron cosputtering and analyzed with automated EDX and XRD to elucidate compositional and structural properties. An automated optical scanning droplet cell was then used to perform photoelectrochemical measurements of 289 compositions on the library, including electrochemical stability, potentiodynamic photocurrents and photocurrent spectroscopy. The photocurrent onset and open circuit potentials of two semiconductor compositions (n-type semiconducting: $Fe_{51}Cr_{47}Al_2Ox$, p-type semiconducting $Fe_{36.5}Cr_{55.5}Al_8O_x$) are favorable for water splitting. Cathodic photocurrents are observed at 1.0 V vs RHE for the p-type material exhibiting an open circuit potential of 0.85 V vs RHE. The n-type material shows an onset of photocurrents at 0.75 V and an open circuit potential of 0.6 V. The p-type material showed a bandgap of 1.55 eV, while the n-type material showed a bandgap of 1.97 eV.

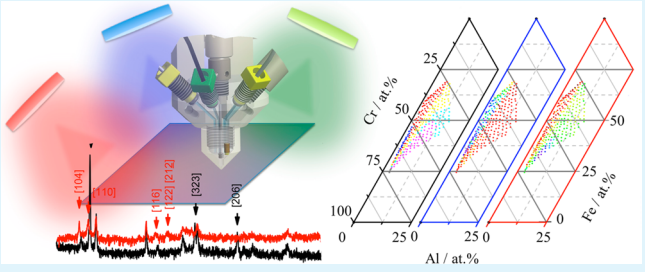

KEYWORDS: *solar water splitting, photoelectrochemistry, materials library, scanning droplet cell, high-throughput characterization, photocurrent*

INTRODUCTION

Discovering and optimizing metal oxide based semiconductor materials for photoelectrochemical water splitting that are abundant, stable and nontoxic is one of the most challenging tasks in modern materials science. Despite increasing efforts in recent years, there is still no material known that ideally matches the necessary criteria for efficient water photoelectrolysis. Up to now only a fraction of all possible metal oxides has been investigated and only a few of them show promising properties for solar water splitting. The predominantly investigated binary oxides Fe_2O_3, TiO_2, and WO_3 do not show sufficient stability, suitable bandgaps, efficient light absorption, catalytic activity, or charge carrier lifetimes.[1]

It is likely that a material for bias-free solar water splitting rather consists of more than two elements, each contributing to the required properties such as stability, light absorption, and catalytic activity.[2−4] There are about 20 000 possible 1:1:1 ternary oxide combinations, if 50 metallic elements are chosen as starting materials and very many more, when various structures and relative compositions are considered. The prediction of all relevant properties of a multicomponent metal oxide material for solar water splitting is still beyond the current capabilities of theoretical models and calculations. Combinatorial material fabrication, with both synthesis and rapid analysis of a large number of compositions in materials libraries and high-throughput characterization, may therefore serve as key method for the discovery and optimization of novel materials compositions and properties.[5,6] To speed up the discovery of new materials a combinatorial method involving inkjet printing of metal oxide precursors in overlapping patterns onto conducting glass substrates followed by annealing at 525 °C was demonstrated.[7] This comparatively simple method was extended to a distributed combinatorial outreach program.[8] Recently, a ternary metal oxide materials library (ML) consisting of codeposited Al, Fe and Cr, investigated using inkjet printing of the related metal nitrate salts, revealed photoactive p- and n-type semiconductors.[9] The p-type oxide is a material with composition $Fe_{0.84}Cr_{1.0}Al_{0.16}O_3$, a bandgap energy of 1.8 eV and an open circuit photovoltage for hydrogen evolution of nearly 1.0 V.

To gain an in-depth knowledge about the photoelectrochemical (PEC) properties of the Fe–Cr–Al–O system, a thin film

Received: December 18, 2014
Accepted: February 4, 2015
Published: February 4, 2015

DOI: 10.1021/am508946e
ACS Appl. Mater. Interfaces 2015, 7, 4883−4889

materials library covering the interesting compositions was fabricated by combinatorial reactive magnetron cosputter deposition, a technique that is capable of producing high-quality thin films. Subsequently, high-throughput characterization of structural and photoelectrochemical properties was performed on measurement regions of the ML exhibiting defined compositions. In order to correlate structural and compositional properties with the photoelectrochemical performance of the materials an automated optical scanning droplet cell (OSDC)[10−13] was used for photoelectrochemical measurements of the electrochemical stability, potentiodynamic photocurrent, and photocurrent spectroscopy on 289 areas of the ML.

EXPERIMENTAL SECTION

Synthesis of the Thin Film Fe−Cr−Al−O Materials Library. The Fe−Cr−Al−O ML was fabricated in a combinatorial magnetron sputtering system (AJA International ATC2200J).[6] The deposition was performed on a square-shaped 75 mm × 75 mm fluorine doped tin oxide (FTO) coated glass substrate by cosputtering from elemental Fe, Cr, and Al targets (99.99%), confocally positioned in the deposition chamber, with a base pressure <2 × 10^{-7} mTorr. The deposition was performed at a constant pressure of 10 mTorr with a continuous reactive gas flow of Ar, 40 sccm, and O_2, 2 sccm (6 N purity). In the cylindrical deposition chamber the azimuthal angle between the sputter targets was 90°, with the Cr and Al targets opposing each other, while the Fe target was positioned in between them. The deposition of Cr and Fe was performed by direct current (DC) magnetron sputtering with a power of 150 W. Al was sputtered with a radio frequency (RF) source at 100 W.

The resulting film thickness was determined to be about 500 nm by measuring the film thickness at the corners of the substrate that were covered during deposition using a profilometer. The film is slightly (∼100 nm) thinner on the Al rich side because of the geometry of the confocal magnetron sources.

There was no intentional substrate heating during deposition. After deposition, the materials library was annealed in air at 525 °C for 90 min with a heating rate of 16 °C/min and a slow cooling rate of 4 °C/min.

High-Throughput Characterization of the Materials Library. The compositional, structural and PEC high-throughput characterization was performed on a rectangular array of 17 by 17 (289) measurement areas, each 4.5 mm × 4.5 mm in size.

Composition and Structure. Compositional analysis was performed by high-throughput energy dispersive X-ray spectroscopy (EDX) at 20 kV acceleration voltage with 100 μm aperture in a JEOL JSM 5800LV equipped with an Oxford Inca system. The crystallographic analysis of the materials library was performed by X-ray diffraction analysis over all measurement regions in Bragg−Brentano diffractometer geometry (Philips X'Pert, PANalytical; Ni-filtered Cu Kα radiation). Phase region identification analysis was performed using the CombiView software.[10]

Photoelectrochemical Properties. The photoelectrochemical (PEC) high-throughput characterization of the ML was performed using an automated optical scanning droplet cell (OSDC). The OSDC contained a Ag/AgCl 3 M KCl/0.5 M $NaClO_4$ double junction reference electrode and a Pt-wire counter electrode and was mounted on a three-axes micropositioning system. The droplet cell can be positioned in all spatial dimensions with a positioning accuracy of about 1 μm. The diameter of a specifically designed polytetrafluoroethylene (PTFE) capillary pressed on the sample surface defines the examined geometric area of the sample (0.785 mm^2), which is connected as working electrode to a potentiostat (Jaissle 1002 PC).

Sample illumination was done by means of a Xe lamp (LC8, Hamamatsu Photonics) coupled to the droplet cell via a poly(methyl methacrylate) (PMMA) light fiber. The effective light intensity, that reaches the material surface, was set to 0.785 mW corresponding to a light intensity of 100 mW/cm^2. A syringe pump supplied the measuring cell with 0.5 M $NaClO_4$ electrolyte solution at pH 4.5. All potentials are referred to the reversible hydrogen electrode (RHE).

The dark open circuit potential (OCP) and OCP shift (ΔOCP) under illumination (at 100 mW/cm^2) were locally measured using the OSDC, whereby the latter was determined as the difference between the OCP under illumination and in the dark. A potential scan with a sweep rate of 1 mV/s with simultaneous light chopping at 0.2 Hz from a starting potential of 1.475 V to an end potential of −0.525 V vs RHE was performed. The current values were measured immediately after opening of the lamp shutter, just before closing of the shutter, immediately after closing of the shutter, and just before opening of the shutter allowing the determination of the peak-photocurrent, steady state photocurrent, peak-dark current, and steady-state dark current during one potential scan. These current measurements allow the determination of (i) whether the material at a certain measurement area is a n- or p-type semiconductor, (ii) the peak photocurrent on-set potential, (iii) the steady-state photocurrent on-set potential, (iv) the potential dependence of the photocurrent, (v) the surface recombination rate, and (vi) possible photo- or potential-induced corrosion processes.

Photocurrent Spectroscopy. Photocurrent spectra on selected measurement regions were recorded using a tunable monochromatic light source (Instytut Fotonowy) equipped with a 150 W Xe lamp, a grating monochromator and appropriate cutoff filters. The photocurrent response was measured as the difference between the averaged current values recorded during 20 s in the dark and the averaged current values recorded during 20 s with an illumination at wavelengths between 300 and 700 nm with 5 nm increments at different bias potentials. The external quantum efficiency (EQE) values for each wavelength were calculated as the ratio of the photocurrent density and the irradiation power density, which was measured with a NOVA II optical power meter equipped with a 3A head (Ophir Optronics).

RESULTS AND DISCUSSION

Compositional and Structural Properties. Compositional analysis of the Fe−Cr−Al−O ML by EDX confirmed a composition spread with 25−75 at. % Cr, 75−25 at. % Fe, and 0−15 at. % Al (Figure 1). On the corresponding 277 measurement regions (excluding the corners of the ternary metal-oxide library), XRD diffraction patterns were recorded for 2θ = 30° to 80° at room temperature. The phase region identification analysis was performed with the help of XRD data k-point clustering. Based on the identified phases, the ML was

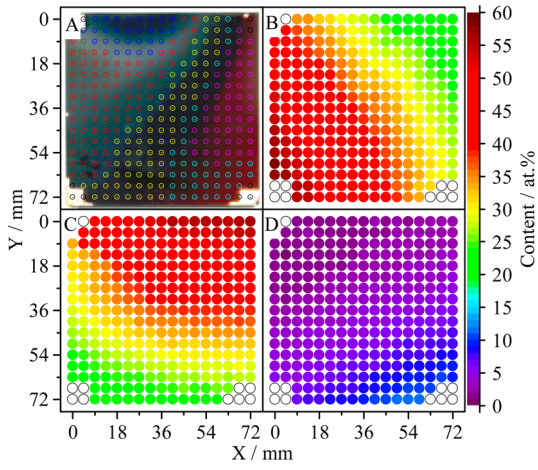

Figure 1. Photograph of the ML with superimposed XRD mapping (A) (see text and Figure 2A) for description of the color-code), EDX mapping of (B) Fe, (C) Cr, and (D) Al with percentages indicated on the color scale.

DOI: 10.1021/am508946e
ACS Appl. Mater. Interfaces 2015, 7, 4883−4889

divided into 5 regions (I–V) suggested by similar XRD patterns. A remarkable similarity of XRD patterns with the optical appearance of the ML can be observed as seen by the colored regions in the optical image of Figure 1A.

In Figure 2A, a color-coded ternary diagram of the identified phases is shown with the colors representing regions (I–V).

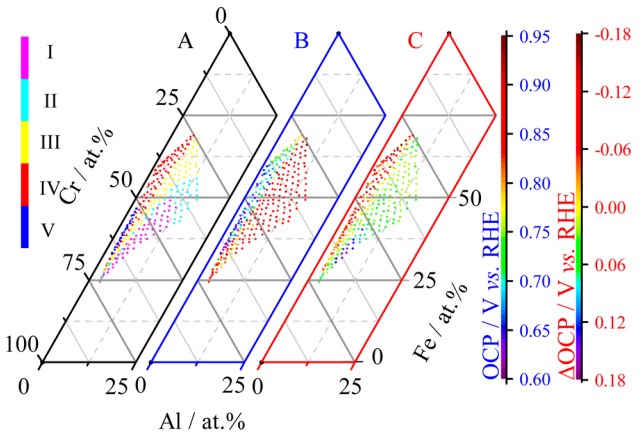

Figure 2. Color-coded visualization of phase regions from XRD maps (A) (black frame, see text for details), dark OCP (B) (blue frame), ΔOCP (C) (red frame), and corresponding color scales.

Figure 1A and Figure 2A share the same color code for illustrating the phase areas in the ML.

The ML showed strong texturing and X-ray fluorescence due to the presence of Fe in the film as well as a shift of peak positions with compositions that limit phase identification. The diffraction peaks in the magenta region I (see Figure 2A) are attributed to a nonstoichiometric Al-doped $Cr_{2-x}Fe_xAl_xO_4$ spinel structure with strong (103) {2Θ = 36.17°} and (206) {2Θ = 76.61°} peaks (Pearson Crystal Database Entry 554776). The peak at 2Θ = 36.17° is the most prominent peak in the whole ML. However, peaks from $Cr_{1.6}Fe_{1.4}O_3$ (Pearson Crystal Database Entry 554776) based on an Al_2O_3 (corundum) structure would also agree with the experimental data.[8] Close to a Cr/Fe ratio of ~2:1, the crystallinity of the films improves making a spinel type structure plausible (see Figure S6, Supporting Information; for the XRD pattern of $Fe_{36.5}Cr_{55.5}Al_8O_x$). The cyan region II shows the same diffraction peaks but with lower intensities. A lower Al content results in smaller peaks in this region. Probably, the lower Al content at a nonstoichiometric composition in this region induces the formation of multiple phases or X-ray amorphous mixtures. The yellow region III shows only diffraction peaks from the substrate. The red region IV and the blue region V have less than 5 at. % Al and the XRD peaks are from a $FeCrO_3$ structure with a substitution with Al. A number of peaks are observed that could be potentially ascribed to the crystal planes (104) {2Θ = 33.28°}, (110) {2Θ = 35.70}, (116) {2Θ = 54.3}, and (122)/(21$\underline{2}$) {2Θ = 57.86} (Pearson Crystal Database Entry 561132). (see Figure S6 Supporting Information; for the XRD pattern of $Fe_{51}Cr_{47}Al_2O_x$). Region V shows higher XRD peak intensities from the same structure indicating a higher crystallinity. This phase region is in agreement with previous observation by Rowley et al.,[9] who detected the same structure in samples made by inkjet printing of metal-nitrate salts.

Open Circuit Potential. In Figure 2A a color-coded ternary diagram of the identified phases is shown, where the colors represent regions (I–V) and the corresponding open circuit potentials in the dark (OCP, Figure 2B) and under illumination (ΔOCP, Figure 2C). The distribution of dark OCPs correlates with the identified dominant phases of the ML as shown in Figure 2A: regions IV and V having <5 at. % Al show OCP values in the range of 0.6 and 0.75 V and are easier to oxidize as compared to materials with an Al content >12 at. %. Regions I–III display dark OCP values between 0.85 and 0.95 V. The transition of dark OCP values between regions I–III and IV–V is very sharp. Since there is a smooth continuous variation of the composition but sharp phase transition, it is presumed that the dark OCP is mainly governed by the crystallinity.

To assess the band structure of different materials within the ML, the OCP shift under illumination was determined. At open-circuit conditions the photogenerated holes or electrons accumulate at the surface in case of n- and p-type semiconducting materials, respectively. The Fermi-level (measured as OCP) hence rises in the case of n-type (ΔOCP is negative) and decreases in the case of p-type semiconductors (ΔOCP is positive).[13,14]

A color-coded ΔOCP ternary diagram is shown in Figure 2C that correlates with the phase constitution of the ML. Regions IV and V show negative ΔOCP values indicating n-type semiconducting properties. The ΔOCP values in these regions vary between −0.035 and −0.17 V. A sharp change in ΔOCP values is observed between regions IV–V and I–III. In regions II and III a negligible influence of illumination on the OCP values was observed. Region I, with <10 at. % Al, showed p-type semiconductor behavior: the ΔOCP was positive in the range from 0.12 to 0.18 V. The part of region I with >10 at. % Al showed no OCP shift upon illumination.

Electrochemical Stability and Photoactivity. Potentiodynamic photocurrent measurements were performed at each measurement area. Figure 3 shows four selected voltammo-

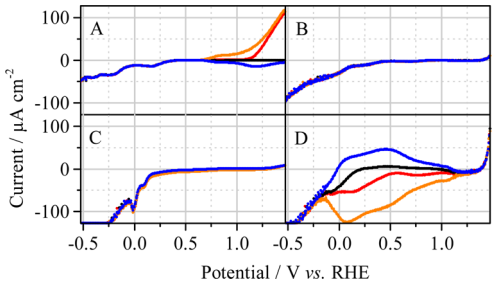

Figure 3. Selected voltammograms recorded within the measurement areas (A) IV/V, (B) III, (C) II and (D) I. Dark current (black lines), peak of dark transient current (blue lines), current under illumination (red lines), and peak of transient photocurrent (orange lines).

grams recorded on region IV/V, Al:$FeCrO_3$ (Figure 3A); region III, noncrystalline Cr_2FeO_3 (Figure 3B); region II, noncrystalline phase with increased Al content (Figure 3C); and region I, Al:Cr_2FeO_x (Figure 3D). Each combined voltammogram shows the dark current (black line), the current under illumination (red line), the peak transient dark current (blue line) and the peak of the photocurrent transient (orange line) as a function of the applied bias potential. The voltammogram recorded on a selected measurement area in region IV/V, Al:$FeCrO_3$, depicted in Figure 3A shows a behavior typical for a n-type semiconductor. The anodic photocurrent onset potential is 1.025 V and the transient photocurrent onset potential is 0.65 V. No anodic dark current was detected in the scanned potential range. The cathodic

DOI: 10.1021/am508946e
ACS Appl. Mater. Interfaces 2015, 7, 4883–4889

current at −0.425 V may indicate reduction of metal sites in the structure. At least three redox peaks were observed at 0.165, −0.24, and −0.4 V.

XRD data of materials in region III suggest noncrystallinity. No photoactivity was detected over the entire range of applied bias potentials (Figure 3B). Similar to region IV, a dark cathodic current was observed at bias potentials <0.425 V. Anodic currents were observed at potentials >1.38 V possibly because of oxidation of the material. Voltammograms recorded on the noncrystalline region II showed negligible photoactivity, whereas strong cathodic currents were observed at potentials <0.25 V most probably caused by reduction of metal ions in the structure (Figure 3C). Region V showed an identical corrosion behavior at bias potentials <0.25 V. However, region V exhibited photoactivity at potentials between −0.14 and 1.25 V. The maximum photocurrent was recorded at a bias potential of 0.22 V. Interestingly, the photoactivity decreased at 0.575 V but increased again at 0.75 V (Figure 3D).

Extracting the photo- and dark current densities at certain potentials for all measured areas is the basis of a map of the current density values within a ternary composition diagram. This was done for three bias potentials: 1.475 V, where the n-type semiconductor materials in regions IV and V showed high photocurrent values (see Figure 3A for region V), as well as at 0.75 and 0.22 V, two potentials at which the material of the composition $Fe_{36.5}Cr_{55.5}Al_8O_x$ (region I) showed maximum photoactivity. The dark current mapping for three bias potentials is shown in Figure 4A−C.

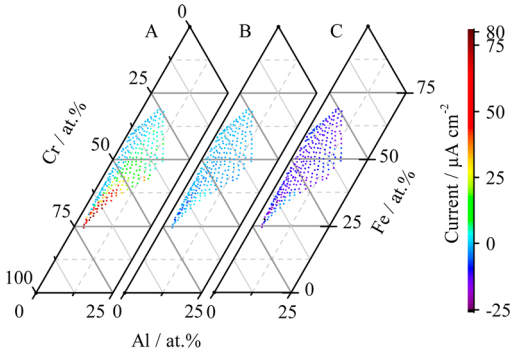

Figure 4. Dark current density maps recorded at (A) 1.475, (B) 0.75, and (C) 0.22 V.

At 1.475 V, region I showed high anodic dark currents (Figure 4A) similar to the corresponding voltammogram (Figure 3D). Regions II and III also corroded anodically. At 0.75 V, small cathodic currents were measured in region II at a Cr concentration >50 at. % (Figure 4B). At 0.22 V, only region I showed low currents, while all other compositions exhibited cathodic currents that increase with increasing Al content (from blue to violet in Figure 4C). Since, the reduction of Al_2O_3 at these potentials can be excluded; we assume that Al is either present in a ternary phase or as substitution in the crystal lattice of the Fe/Cr oxides that can be reduced from higher to lower oxidation states at acidic conditions. Figure 5A−C shows color-coded photocurrent maps for different applied bias-potentials in the ternary composition diagrams. At 1.475 V regions IV and V generated photocurrents of up to 130 $\mu A/cm^2$, while all other regions showed negligible photoactivity. The cathodic current appearing in region I was considered to be noise caused by high dark currents at 1.475 V (Figure 5A). Region I was photoactive

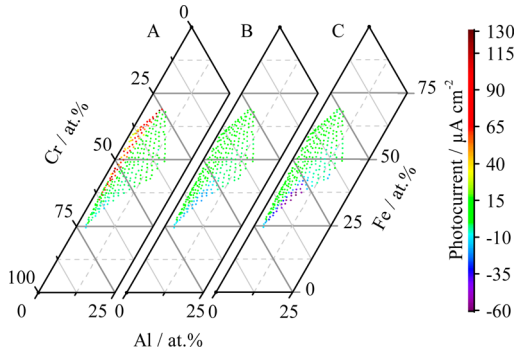

Figure 5. Steady-state photocurrent density maps recorded at (A) 1.475, (B) 0.75, and (C) 0.22 V.

at 750 mV (see also Figure 3D) and generated photocurrents of up to −15 $\mu A/cm^2$. All other regions of the ML were not photoactive. At a bias potential of 0.22 V a stable photocurrent was generated in region I that increases to up to −60 $\mu A/cm^2$ (Figure 5C). The photocurrent maps correspond well to the ΔOCP map where regions IV and V have n-type semiconductor properties and region I has p-type semiconductor properties, whereas no photoactivity was detected in the other regions.

Quantum Efficiency and Estimated Bandgaps. The measurement areas that generated the highest photocurrent densities from regions IV−V with the composition $Fe_{51}Cr_{47}Al_2O_x$ and from region I with the composition $Fe_{36.5}Cr_{55.5}Al_8O_x$ (n- and p-type semiconductors, respectively) were selected for further photocurrent spectroscopy studies. The best performing p-type semiconductors were found in a relatively narrow compositional range. The n-type materials, however, show similar high photocurrents over a broad composition range ($Fe_{(36-68)}Cr_{(62-26)}Al_{(2-6)}$, Figure 5A).

Photocurrent spectra were recorded at different applied bias potentials within the corresponding electrochemical stability windows determined from the potential dependent photocurrent measurements (Figure 3). The n-type semiconductor potential window was between 0.55 and 1.65 V, while the p-type semiconductor was investigated in a potential range between 1.3 and 0 V. The incident photon to current efficiency (IPCE) spectrum of a selected n-type semiconductor is shown as a function of wavelength and applied bias potential in Figure 6. The ratio of the current and irradiance for each wavelength was calculated and $(EQE/(1\text{-}EQE)*h\nu)^s$ versus $h\nu$ plots with s = 0.5 and 2 were used to determine the transition type and bandgap values of the materials as shown in Figure 7.[14,15] Usually Tauc plots are used to interpret absorbance data. In the case of photocurrent data the carrier transport is contributing by both diffusion and due to the space charge thickness which complicates the analysis. The IPCE spectrum of the selected p-type semiconductor is shown in Figure 8 and the corresponding Tauc plot in Figure 9.

n-Type Semiconductor. Figure 6 shows the external quantum efficiency (EQE) as a function of wavelength and applied bias potential. Below 0.7 V, no photoactivity was observed. Between 0.75 and 1.25 V the photocurrent onset was between 350 and 375 nm, while at bias potentials >1.25 V the photocurrent onsets shifts between 475 and 500 nm. The maximum observed EQE at 1.65 V and 240 nm was about 8.2%. Extrapolation of the linear region of the $(EQE/(1\text{-}EQE)*h\nu)^{1/2}$ versus $h\nu$ plot leads to an indirect E_g of 1.97 ±

DOI: 10.1021/am508946e
ACS Appl. Mater. Interfaces 2015, 7, 4883−4889

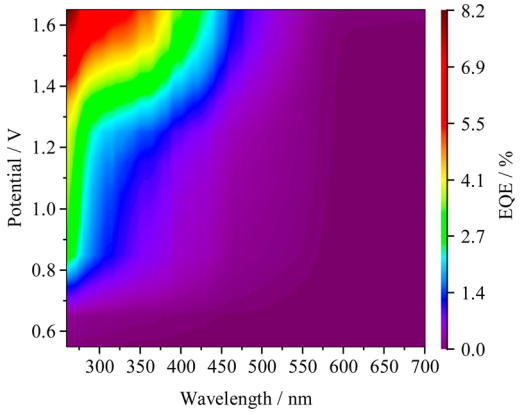

Figure 6. EQE spectra of the n-type semiconducting material calculated from photocurrent spectra acquired at different bias potentials.

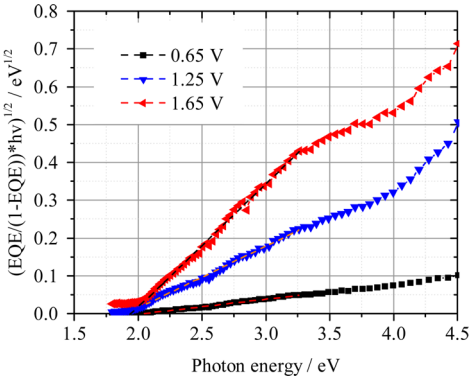

Figure 7. Tauc-type plots $(EQE/(1\text{-}EQE)*h\nu)^{1/2}$ versus $h\nu$ of the n-type semiconducting material.

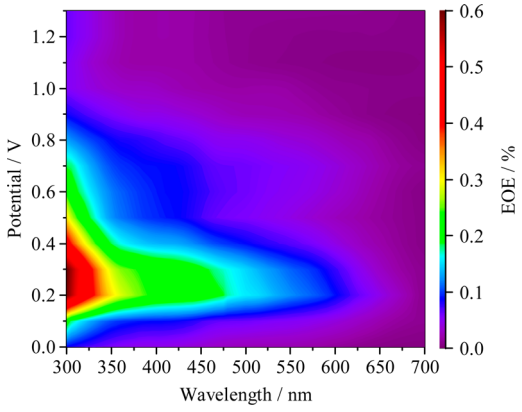

Figure 8. EQE spectra of the p-type semiconducting material calculated from photocurrent spectra acquired at different bias potentials.

0.07 eV, which is not depending on the applied bias potential (Figure 7). The carriers with very short diffusion lengths generated deeper in the material cannot be collected unless the space charge layer is expanded into the material by application of rather high bias potential values. This explains the apparent extension of the absorption spectrum at higher applied bias potentials.

p-Type Semiconductor. Prior to spectra acquisition, the photoelectrochemical cell has been purged with Ar and it was continuously purged with H_2 during the measurement in order

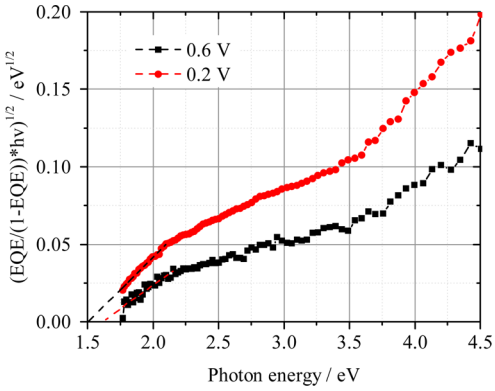

Figure 9. Tauc-type plots $(EQE/(1\text{-}EQE)*h\nu)^{1/2}$ versus $h\nu$ of p-type semiconducting material.

to maintain the reduction potential of the protons.[1] In correspondence to observations of Rowley et al.,[9] the steady-state photocurrent was not completely reached after 20 s illumination, whereby the initial peak transient current was 100 times higher as after 20 s, which clearly indicates significant charge recombination occurring in this material that is not surprising given that the surface has no catalyst for hydrogen evolution.[17]

This explains the much lower EQE of the p-type material as compared to that of the n-type material even though the photocurrents estimated by potentiodynamic current measurement were comparable. EQE values in dependence from the wavelength and applied bias potential for the selected p-type semiconducting material are shown in Figure 8.

This material composition exhibits a broad absorption range. At 0.5 V the absorption range extends to 450 nm, however, between 0.2 and 0.7 V the absorption range extends to 650 nm (see also Figure 3D). The sharp onset of the EQE spectrum at 0.4 V in Figure 8 could be explained by Fermi level pinning from where a space charge layer grows again. The drop in EQE at 0.2 V could be attributed to photoelectrochemical self-reduction of most probably Fe(III) to Fe(II). From the Tauc-type plot a bandgap value of 1.55 ± 0.05 eV can be determined.

CONCLUSIONS

A comprehensive high-throughput study of a reactive magnetron cosputtered Fe−Cr−Al−O material library was performed to evaluate the suitability of Al−Cr−Fe−O as a solar water splitting material. The fabricated Fe−Cr−Al−O ML shows photoactive regions, which were identified by an automated scanning droplet cell with linear sweep voltammetry under chopped light. The identified n- and p-type areas show promising photocurrent onset potentials and high OCP. The identified n-type material $Fe_{51}Cr_{47}Al_2O_x$ has a peak-photocurrent on-set potential of 0.7 V and a steady-state photocurrent on-set potential of 1.1 V. This composition generates a photocurrent of up to 130 $\mu A/cm^2$ at 1.43 V bias potential and has an indirect bandgap with an energy level equal to 1.94 eV. The maximal EQE value is 8.2% at 240 nm and 1.65 V bias potential in absence of a cocatalyst for oxygen evolution on its surface.

A second photoactive material was identified having the composition $Fe_{36.5}Cr_{55.5}Al_8O_x$. It has p-type semiconductor behavior with and indirect bandgap of 1.6 eV generating up to −60 $\mu A/cm^2$ photocurrent, whereby substantial surface recombination was observed. The maximal EQE value was

DOI: 10.1021/am508946e
ACS Appl. Mater. Interfaces 2015, 7, 4883−4889

0.6% at 300 nm and 0.3 V bias potential. Both materials possess suitable bandgaps and photoelectrochemical properties required to construct a tandem photoelectrolysis device.[18]

The materials found agree well with the previous materials compositions found by Rowley et al.,[9] however, at slightly different compositions. XRD data indicate that the identified p-type ternary-metal oxide has a spinel structure. The n-type material seems to be of Al_2O_3 type structure. Differences in the phase composition might be expected due to the different preparation techniques and annealing conditions.

Slightly Fe-rich areas act as n-type semiconductor (Fe/Cr ratio of ~2:1) while regions with more Cr act as p-type semiconductor (Cr/Fe ratio of ~2:1). There is a region with a Fe/Cr ratio of ~1:1 which is not photoactive. This doping behavior could be explained by A-site substitution of cations in an A_2BO_4 spinel type structure. As indicated by the XRD data there could be a mixture of different quasi-binary spinel type crystals that lead to beneficial electronic structures for solar water splitting. In the p-type area at high Cr and Al concentrations a Cr_2FeO_4 structure seems to be formed whose diffraction patterns decrease rapidly for off-stoichiometry from a Cr/Fe = 2:1 ratio. It is possible to substitute the A and B sites in a spinel-type structure when moving along a horizontal line in a ternary diagram suggesting a doping effect of Al.

The p-type semiconductor properties could be explained by the substitution of A site cations as Cr_2FeO_4 is an intrinsic p-type semiconductor of doping type four (DT-4). Substitution of Cr^{2+} by Al^{3+} should increase p-doping and hence conductivity. The absence of a photoelectrochemical effect in undoped and nonstoichiometric Cr_2FeO_4 could be due to the electrical inactiveness of such DT-4 semiconductors. The n-type material is found to be of $FeCrO_3$:Al structure. The doping behavior could be due to the lower ion radius of Al as compared to Cr and Fe leading to a compression type distortion of the lattice that could act as additional n-doping. The remarkable high photocurrent onset potential of the identified p-type material makes this system an interesting candidate material for solar water splitting. The materials are however in an early stage of development. By considering the bandgaps of the best n- and p-type materials (1.6 and 2.0 eV) a maximum theoretical efficiency of up to 18% solar to hydrogen could be achieved.[16] As these materials are known stable oxides with a corundum type crystal structure they should show decreased corrosion as compared with the currently best performing materials based on III–IV semiconductors.[17] Testing of an actual optimized tandem cell device is subject for future research on this materials system.

■ ASSOCIATED CONTENT

Supporting Information

Schematic of the measurement setup, normalized direct Tauc plot for the p-type material; normalized direct Tauc plot for the n-type material; normalized indirect Tauc plot for the p-type material; normalized indirect Tauc plot for the n-type material; XRD patterns of the p- and n-type materials. This material is available free of charge via the Internet at http://pubs.acs.org.

■ AUTHOR INFORMATION

Corresponding Authors

*E-mail:: alfred.ludwig@rub.de.

*E-mail: wolfgang.schuhmann@rub.de.

Author Contributions

K.S. and H.S.S. contributed equally.

Funding

The authors are grateful to the DFG for the financial support within the SPP1613 (Schu929/12-1, LU1175/10-1). K.S. and H.S.S. acknowledge PhD fellowships by the International Max Planck Research School for Surface and Interface Engineering (IMPRS-SurMat). B.A.P acknowledges the Division of Chemical Sciences, Geosciences, and Biosciences, Office of Basic Energy Sciences of the U.S. Department of Energy through Grant DE-FG02-05ER15750 for funding.

Notes

The authors declare no competing financial interest.

■ ACKNOWLEDGMENTS

Dr. Yahya Motemani is acknowledged for his help in performing XRD measurements.

■ REFERENCES

(1) Walter, M. G.; Warren, E. L.; McKone, J. R.; Boettcher, S. W.; Mi, Q.; Santori, E. A.; Lewis, N. S. Solar Water Splitting Cells. *Chem. Rev.* **2010**, *110*, 6446–6473.

(2) Alexander, B. D.; Kulesza, P. J.; Rutkowska, I.; Solarska, R.; Augustynski, J. Metal Oxide Photoanodes for Solar Hydrogen Production. *J. Mater. Chem.* **2008**, *18*, 2298–2303.

(3) Osterloh, F. E.; Parkinson, B. A. Recent Developments in Solar Water-splitting Photocatalysis. *MRS Bull.* **2011**, *36*, 17–22.

(4) Schoonman, J.; Krol, R. v. d. Nanostructure Materials for Solar Hydrogen Production. *Sci. Bull.—Univ. "Politeh." Bucharest, Ser. B* **2011**, *73*, 31–44.

(5) Ludwig, A.; Cao, J.; Brugger, J.; Takeuchi, I. MEMS Tools for Combinatorial Materials Processing and High-Throughput Characterization. *Meas. Sci. Technol.* **2005**, *16*, 111–118.

(6) Ludwig, A.; Zarnetta, R.; Hamann, S.; Savan, A.; Thienhaus, S. Development of Multifunctional Thin Films Using High-throughput Experimentation Methods. *Int. J. Mater. Res.* **2008**, *99*, 1144–1149.

(7) Woodhouse, M.; Parkinson, B. A. Combinatorial Approaches for the Identification and Optimization of Oxide Semiconductors for Efficient Solar Photoelectrolysis. *Chem. Soc. Rev.* **2009**, *38*, 197–210.

(8) Anunson, P. N.; Winkler, G. R.; Winkler, J. R.; Parkinson, B. A.; Schuttlefield Christus, J. D. Involving Students in a Collaborative Project To Help Discover Inexpensive, Stable Materials for Solar Photoelectrolysis. *J. Chem. Educ.* **2013**, *90*, 1333–1340.

(9) Rowley, J. G.; Do, T. D.; Cleary, D. A.; Parkinson, B. A. Combinatorial Discovery Through a Distributed Outreach Program: Investigation of the Photoelectrolysis Activity of p-Type Fe, Cr, Al Oxides. *ACS Appl. Mater. Interfaces* **2014**, *6*, 9046–9052.

(10) Khare, C.; Sliozberg, K.; Meyer, R.; Savan, A.; Schuhmann, W.; Ludwig, A. Layered WO_3/TiO_2 Nanostructures with Enhanced Photocurrent Densities. *Int. J. Hydrogen Energy* **2013**, *38*, 15954–15964.

(11) Fan, M.; Sliozberg, K.; La Mantia, F.; Miyashita, N.; Hagymási, M.; Schnitter, C.; Ludwig, A.; Schuhmann, W. Characterization of Ta–Ti Thin Films by Using a Scanning Droplet Cell in Combination with AC Linear Sweep Voltammetry. *ChemElectroChem* **2014**, *1*, 903–908.

(12) Stepanovich, A.; Sliozberg, K.; Schuhmann, W.; Ludwig, A. Combinatorial Development of Nanoporous WO_3 Thin Film Photoelectrodes for Solar Water Splitting by Dealloying of Binary Alloys. *Int. J. Hydrogen. Energy* **2012**, *37*, 11618–11624.

(13) Sliozberg, K.; Meyer, R.; Ludwig, A.; Schuhmann, W. A Combinatorial Study of Photoelectrochemical Properties of Fe–W–O Thin Films. *ChemPlusChem* **2015**, *80*, 136–140.

(14) Tauc, J.; Grigorovici, R.; Vancu, A. Optical Properties and Electronic Structure of Amorphous Germanium. *Phys. Status Solidi B* **1966**, *15*, 627–637.

DOI: 10.1021/am508946e
ACS Appl. Mater. Interfaces 2015, 7, 4883–4889

(15) Kam, K. K.; Parkinson, B. A. Detailed Photocurrent Spectroscopy of the Semiconducting Group VI_B Transition Metal Dichalcogenides. *J. Phys. Chem.* **1982**, *86*, 463−467.
(16) Döscher, H.; Geisz, J. F.; Deutsch, T. G.; Turner, J. A. Sunlight Absorption in Water—Efficiency and Design Implications for Photoelectrochemical Devices. *Energy Environ. Sci.* **2014**, *7*, 2951−2956.
(17) Khaselev, O.; Turner, J. A Monolithic Photovoltaic-Photoelectrochemical Device for Hydrogen Production via Water Splitting. *Science* **1998**, *280*, 425−427.

DOI: 10.1021/am508946e
ACS Appl. Mater. Interfaces 2015, 7, 4883−4889